

# Stark Localisation Notes

Christian Duffin

July 6, 2022

## Contents

<b>1</b>	<b>Wannier-Stark Localisation</b>	<b>2</b>
<b>2</b>	<b>Stark Many-Body Localisation</b>	<b>5</b>
2.1	Level Statistics . . . . .	6
2.2	Entanglement Entropy . . . . .	9
<b>3</b>	<b>Driven Wannier-Stark Localisation</b>	<b>12</b>
3.1	Dynamics . . . . .	12
3.2	IPRs . . . . .	14
3.3	Localisation Length . . . . .	15
3.4	Degeneracies Induced by Periodic Driving . . . . .	17
<b>4</b>	<b>Driven Stark Many-Body Localisation</b>	<b>18</b>
4.1	IPRs . . . . .	19
4.2	Multifractality . . . . .	22

4.3	Dynamics . . . . .	25
4.4	Driven Field vs Driven Hopping . . . . .	26
4.5	Alternative Driving . . . . .	28

## 1 Wannier-Stark Localisation

It is generally understood that disorder is a necessary precondition for localisation in quantum systems. With this in mind, one natural question might be whether it is possible for a quantum system to be localised without disorder. Shortly after Anderson's original paper regarding single-particle localisation on a disordered lattice, a similar phenomenon was demonstrated in a system without disorder [1]. Here, eigenstates are exponentially localised under the action of external fields, exhibiting what is now known as Wannier-Stark localisation.

A simple single-particle system that we can invoke is the 1D Anderson model, with disorder mean and variance set to 0. This system can be expressed as follows:

$$H = J \sum_j (c_j^\dagger c_{j+1} + \text{h. c.}). \quad (1)$$

In this system, there is nothing to distinguish the energies of each configuration from each other. As a result, the eigenenergies are exactly degenerate, and the contribution of each basis state to each eigenstate is equal. This system is thus maximally delocalised for all non-zero  $J$ .

These degeneracies can be lifted under the presence of an external, non-uniform field. The simplest of such fields is a linear, 'tilted' potential [2, 3]. Adding this to the Hamiltonian, we have

$$H = J \sum_j (c_j^\dagger c_{j+1} + \text{h. c.}) + \sum_j W_j c_j^\dagger c_j. \quad (2)$$

Here, the potential is defined as

$$W_j = -\gamma j. \quad (3)$$

The maximum magnitude of this potential is  $\gamma L$ , at the right-most site of the lattice. We can therefore state that the potential has a negligible impact on the Hamiltonian in the limit  $\gamma L \ll J$  (which is just  $\gamma = 0$  in the thermodynamic limit). Setting  $J = 0$ , the basis states become eigenstates of the Hamiltonian, and thus the energy difference between adjacent eigenvalues is

equal to  $\gamma$  throughout the entire spectrum. For non-zero  $J$ , and away from the  $\gamma L \ll J$  limit, the energy difference is equal to  $\gamma$  throughout the spectral bulk, while the influence of the hopping elements is limited to the edges.

Similar to our treatment of the Anderson model, we can plot the average eigenvector structure of this model across the lattice sites. Figure 1 shows the average distribution of eigenvector weights for various choices of potential gradient,  $\gamma$ .

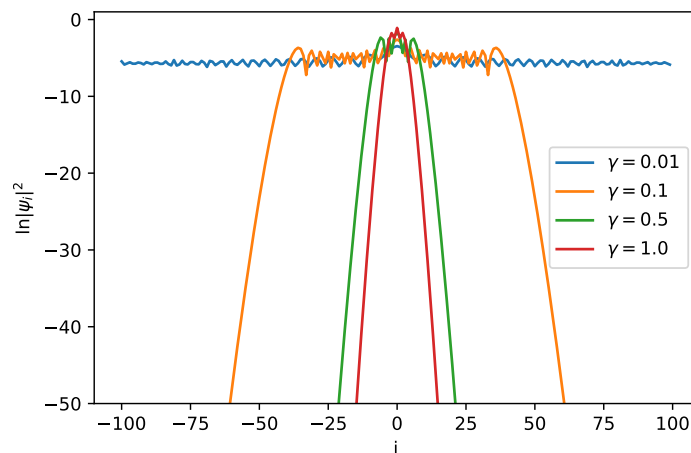


Figure 1: Average distribution of log of eigenvector weights across real space, centred around site with largest weight. Parameters are  $L = 200$ ,  $J = 1$ .

At  $\gamma = 0.01$ , we can see that the system is strongly delocalised, indicating the effective abundance of degeneracies. This corresponds to the limit in which the potential has a negligible amplitude, where  $\gamma L \ll J$ . At  $\gamma = 1$ , the eigenstates are exponentially localised around very few sites, similar to Anderson localisation. What makes this picture unusual, however, is the behaviour seen at intermediate  $\gamma$ . At  $\gamma = 0.1$ , the eigenstates are equally distributed across a finite fraction of lattice sites, beyond which there is a sudden exponential decay. Qualitatively, this can be explained by the fact that groups of basis states that are separated by a small number of particle hops possess energy differences that are small relative to  $J$ . Effectively, this means that the system is  $l$ -fold degenerate, with  $l < L$ .

Taking various system sizes, we find numerically that  $l$  is size-independent, which ensures that

the fraction  $l/L$  converges towards 0 with increasing system size. This is quite intuitive if one considers that increasing  $L$  simply amounts to increasing the size of the region that the eigenvectors have no support in. This implies that the degenerate region constitutes a vanishing fraction of real space in the thermodynamic limit, and confirms that the intermediate region of parameter space seen in figure 1 collapses into the critical point between a maximally delocalised (degenerate) phase and an exponentially localised phase. We can therefore assume that the system is exponentially localised in all regions in parameter space, with the exception of the trivially delocalised  $\gamma L \ll J$  region.

One should also note that the behaviour seen when averaging over all eigenvectors might not be representative of the eigenvectors in general, but could instead be dominated by a subset of vectors with extreme properties. To check this, we can plot the data for all eigenvectors individually.

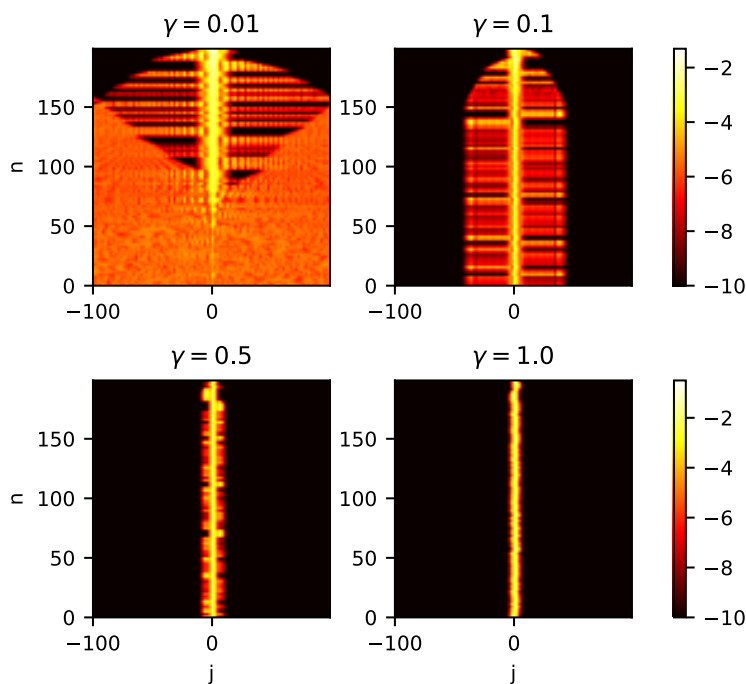


Figure 2: Heatmap plot of log of all eigenvector weights,  $\ln |\psi_j^{(n)}|^2$ , where  $j$  denotes position in real space and  $n$  denotes the  $n$ th eigenvector. These eigenvectors correspond to the averages seen in figure 1 for each choice of  $\gamma$ , and have all been shifted such that the location of maximum weight is at  $j = 0$ . All weights below -10 have been truncated to -10 for clarity.

In figure 2, we plot every eigenvector individually for the same choices of  $\gamma$  as in figure 1. At  $\gamma = 0.01$ , some of the eigenvectors look significantly more localised. This is consistent with the fact that eigenvectors towards the spectral edges tend to look more localised than those seen in the spectral bulk. At larger  $\gamma$ , it can be seen that little variation exists between eigenvectors, indicating that the average is representative of the eigenvectors in general.

## 2 Stark Many-Body Localisation

As previously discussed, the generalisation of Anderson localisation to many-body interacting systems is known as many-body localisation. It is therefore natural to ask at this point whether Wannier-Stark localisation can also be generalised in this way. This so-called Stark MBL has recently been demonstrated to exist in a system of spinless fermions [2], and in the Heisenberg chain [3]. Here, the presence of a tilted potential results in eigenstates that exhibit the usual non-ergodic features strongly associated with MBL systems. This includes Poisson level statistics, logarithmic entanglement spreading and subdiffusive transport around the ergodic side of the MBL transition point.

The robustness of Stark localisation in the presence of interactions has been demonstrated via exact diagonalisation of small chains [4] and the non-linear Schrödinger equation [5]. Recent work has attempted to put Stark MBL on a theoretical footing, in terms of Hilbert space shattering [6] and Hilbert space fragmentation [7–9]. Experimental work regarding Stark MBL has also recently emerged, including its observation in a superconducting quantum processor [10], a two-dimensional tilted system [11] and a one-dimensional system [12]. The long-time stability of Stark MBL has also been investigated [12–18]. A recent work suggests for any gradient  $\gamma$ , a system will always delocalise after an initial time that scales exponentially with system size. This therefore suggests that a system is only truly localised in the thermodynamic limit [19].

In order to extend our Hamiltonian to the description of a many-body system, let us add a nearest-neighbour interaction term:

$$H = J \sum_j (c_j^\dagger c_{j+1} + \text{h. c.}) + \sum_j W_j c_j^\dagger c_j + V \sum_j n_j n_{j+1}, \quad (4)$$

where  $V$  is the strength of interactions, and  $n_j n_{j+1}$  ensures interactions between nearest-neighbours only. Here, it is also important to clarify which type of particle exists on the lattice. If we are

to ensure that each lattice site only permits one particle at a time, then we should take the particles to be either hard-core bosons or fermions. In either case, the Fock basis will be the same. However, in bosonic systems, the creation and annihilation operators obey the following commutation relations:

$$[b_i, b_j^\dagger] = \delta_{i,j}, [b_i^\dagger, b_j^\dagger] = [b_i, b_j] = 0, \quad (5)$$

whereas those of fermionic systems obey the analogous anticommutation relations:

$$\{f_i, f_j^\dagger\} = \delta_{i,j}, \{f_i^\dagger, f_j^\dagger\} = \{f_i, f_j\} = 0. \quad (6)$$

For our purposes, we will be taking the particles to be hard-core bosons, such that  $c_i = b_i$ . We will also half-fill the lattice for any given size, giving a particle number  $N = L/2$ , and a dimensionality derived from the binomial coefficient:

$$\mathcal{D} = \binom{L}{L/2}. \quad (7)$$

## 2.1 Level Statistics

To investigate the MBL properties of this system numerically, let us first take a look at the level statistics, invoking the usual adjacent spacing ratio [20]. Here, we will also introduce a curvature term to the potential:

$$W_j = -\gamma j + \alpha j^2 / L^2. \quad (8)$$

The second term is a quadratic term that causes the amplitude to curve towards 0 as one moves towards the RHS of the chain [2]. The purpose of adding this non-uniformity to the field will become apparent shortly.

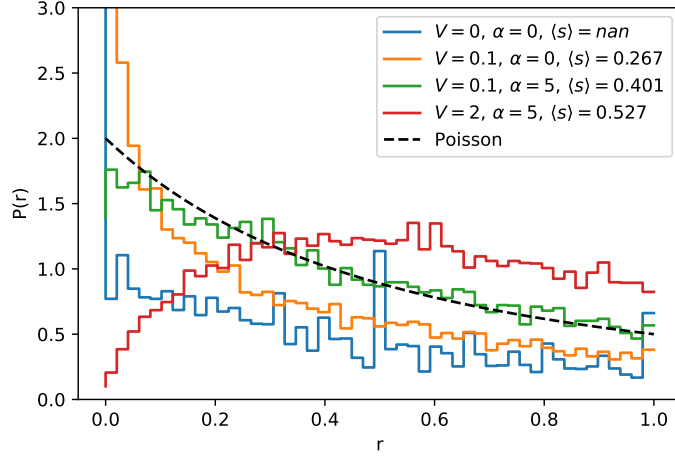


Figure 3: Probability distribution of the adjacent spacing ratio for a curved potential, defined in equation 8. Parameters are  $L = 16$ ,  $J = 1$ ,  $\gamma = 1$ . The Poisson prediction for a localised/integrable system has been added for comparison, defined as  $P_P(r) = 2/(1+r)^2$ .

The results for the level statistics are presented in figure 3. At  $V = \alpha = 0$ , the distribution is seen to peak disproportionately at  $r = 0$ , and the mean falls well below the Poisson value. This occurs because all states that share the same centre of mass are degenerate, where the corresponding eigenvalues are constructed from a set of  $-\gamma j$  terms whose sums are equal. Adding a weak interaction to the Hamiltonian – such that  $V \ll \gamma$  – breaks these degeneracies, but only by splitting them into narrow bands whose widths are small relative to the distance between the bands. As a consequence, the level statistics still exhibit a strong signature of degeneracy at  $V = 0.1$ ,  $\alpha = 0$ . An example of this splitting is demonstrated for a small system in figure 4.

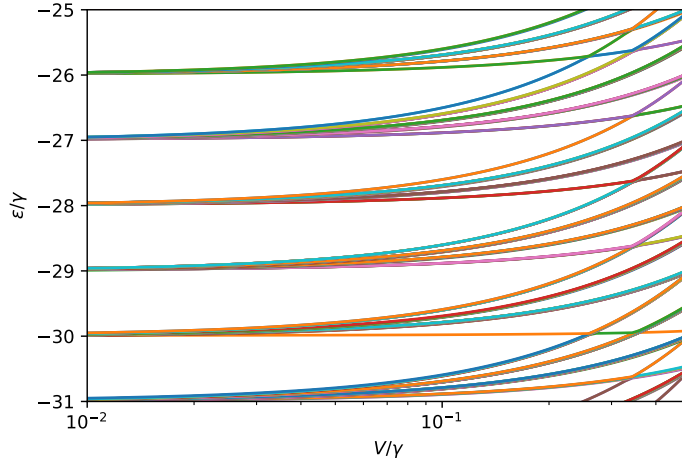


Figure 4: Demonstration of the splitting of degenerate energy levels into bands as the interaction strength  $V$  is increased in a system with a uniform, tiled potential. Parameters are  $L = 12$ ,  $J = 1$ ,  $\gamma = 10$ .

Of course, having a distribution that deviates away from the Poisson and Wigner-Dyson forms eliminates our ability to observe whether the system is localised or delocalised. Nonetheless, from the above argument we know that the non-interacting system possesses exact degeneracies, which are broken by the addition of finite  $V$ . If we wish to address this in terms of perturbation theory – in which  $V$  is a perturbation applied to the non-interacting system – then one has to invoke degenerate perturbation theory so as to avoid the divergences yielded by the equal eigenvalues. What one then discovers is that each set of degenerate eigenstates contribute equally to any given perturbed eigenstate as a linear superposition. As such, these eigenstates are strongly hybridised, which ensures that Wannier-Stark localisation is destroyed in the presence of interactions.

However, if one introduces a degree of non-uniformity to the field, then the exact degeneracies in the non-interacting case are destroyed, and the eigenstates are no longer hybridised in the addition of interactions. The effect of adding this non-uniformity is demonstrated in figure 3 with the factor  $\alpha = 5$ . At  $V = 0.1$ , the distribution agrees quite well with the Poisson prediction, whereas at  $V = 2$  there is a strong tendency towards the Wigner-Dyson form. This implies the existence of a phase transition at finite  $\gamma$ , as has been suggested in previous exact diagonalisation studies [4].



It should also be noted that the effect of adding non-uniformity to the field can alternatively be achieved by adding random on-site disorder, with a small enough variance that it does not induce standard MBL.

The phenomenology discussed in this section is summarised in the table below.

$V/\gamma$	$\alpha$	Loc/Deloc.	Level Statistics	Reason for Loc/Deloc.
0	0	Loc.	Degenerate (exact)	Wannier-Stark localisation
Small	0	Deloc.	Degenerate (approx.)	Hybridised eigenstates
Small	Finite	Loc.	Poisson	Curvature breaks degeneracies
Large	Finite	Deloc.	Wigner-Dyson	Large $V/\gamma$

## 2.2 Entanglement Entropy

Another well-known signature of localisation in a many-body system is entanglement entropy growth. In a thermal system, the entropy is known to exhibit volume law scaling, which corresponds to a linear dependence on the system size  $L$ , as well as ballistic operator growth across time. Conversely, a system with MBL eigenstates exhibits area law scaling, which corresponds to logarithmic operator growth.

Recall that in a closed system, one can calculate entanglement entropy by considering a subsystem within the full system, and observing how it is coupled to the rest of the system. The system can therefore be thought of two subsystems  $A$  and  $B$ , with respective Hilbert bases  $\mathcal{H}_A$  and  $\mathcal{H}_B$ . These bases relate to that of the full system via

$$\mathcal{H} = \mathcal{H}_A \otimes \mathcal{H}_B. \quad (9)$$

The density matrix of subsystem  $A$  is obtained from the full density matrix by tracing out the states of subsystem  $B$ , i.e.

$$\rho_A = \text{Tr}_B[\rho]. \quad (10)$$

From this, the entanglement entropy of subsystem  $A$  is defined as

$$S = -\text{Tr}[\rho_A \ln \rho_A]. \quad (11)$$

Note also that for the remainder of this section, we will be replacing the curvature term in the titled potential with a disorder term, with amplitude  $w$ . The advantage of this is that the

degeneracies in the non-interacting limit are still negated, but the dependence on  $L$  is eliminated such that extrapolating to the thermodynamic limit can be made clearer. It is also obviously important that  $w \ll \gamma$ , or else we introduce the possibility of the regular disorder-induced MBL. The updated Hamiltonian is thus

$$H = J \sum_j^{L-1} (b_j b_{j+1}^\dagger + \text{h. c.}) + V \sum_j^{L-1} n_j n_{j+1} + \sum_j^L W_j n_j + \sum_j^L \epsilon_j n_j. \quad (12)$$

Here,  $\epsilon_j$  are random numbers drawn from a normal distribution with mean 0 and standard deviation  $w$ .

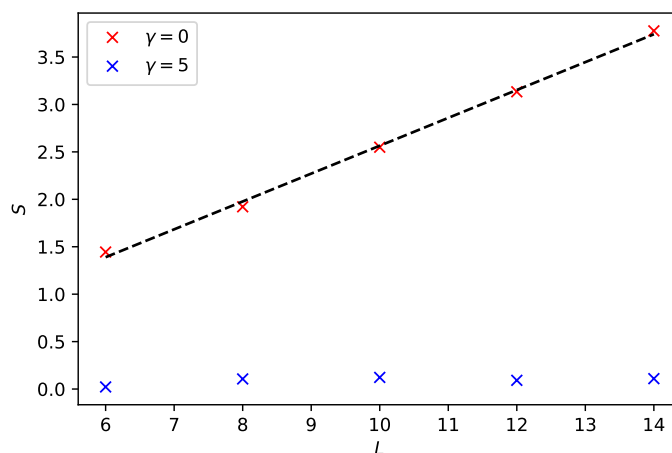


Figure 5: Bipartite entanglement entropy averaged over the middle third of eigenvectors, for field strengths  $\gamma = 0$  and  $\gamma = 5$  which correspond to delocalisation and localisation, respectively. Other parameters are:  $J = V = 0.5$ ,  $w = 0.05$ .

In our case, we will calculate the entanglement entropy after preparing the system in an eigenstate, and average over the middle third of these eigenstates. Specifically we will calculate the bipartite entanglement entropy, in which the subsystems  $A$  and  $B$  correspond to the left and right halves of the system, respectively. Figure 5 demonstrates the dependence on  $L$  for a system in both the localised and delocalised regimes. In the localised case, we effectively see no dependence on  $L$ , whereas in the delocalised case a clearly linear behaviour is seen.

We can also investigate this measure dynamically by preparing the system away from a stationary state, for example a Fock state. Ideally, one would average over several initial states in order

to obtain a statistical average of the time evolution. Selecting all states that possess the same number of domain walls is a particularly appropriate choice, as it is known that Stark MBL is strengthened as the number of domains decreases. The reason for this is related to the mechanisms of Hilbert-space shattering [6], and fragmentation [7, 21]. In our case, we will select all initial states for which the number of domain walls is  $N = L - 3$ .

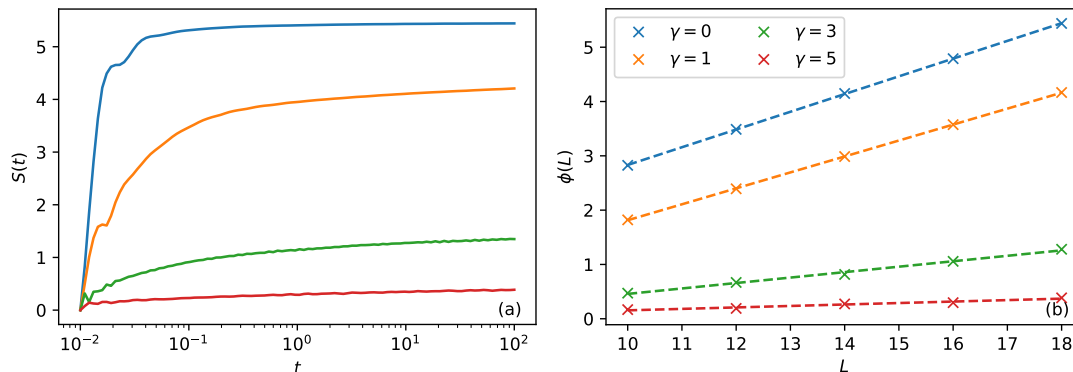


Figure 6: (a) Time evolution of bipartite entanglement entropy averaged over all initial states with number of domain walls  $N = L - 3$ , for system size  $L = 18$ . (b) Saturation point  $\phi(L)$  of entanglement entropy, defined as the entropy averaged over the last 20 time increments in (a). Dashed lines indicate linear interpolations. Other parameters for both plots are:  $J = V = 0.5$ ,  $w = 0.05$ .

From figure 6(a), we see the time evolution for various field strengths. In generic MBL systems, one expects that the entanglement entropy grows logarithmically before reaching its saturation point, whereas in thermal systems it is expected to grow linearly. In our case, it is clear that the growth is slower for larger  $\gamma$ , but whether it is linear or logarithmic is too ambiguous in order to determine whether the system is localised or delocalised. However, another clear property is that the saturation value is shown to decrease for increasing  $\gamma$ . Similarly to figure 5, we could check how this saturation value depends on system size. The difference in this approach from figure 5 is that we will employ dynamics to determine the saturation point  $\phi(L)$  for every  $L$  and  $\gamma$ , which will enable us to determine it at larger sizes.

Figure 6(b) shows the  $\phi(L)$  for increasing system size. As in figure 5, the saturation point clearly increases linearly with  $L$ , indicating volume law scaling. Meanwhile at  $\gamma = 6$ ,  $\phi(L)$  appears to

be  $L$ -independent, which indicates area law scaling.

### 3 Driven Wannier-Stark Localisation

When investigating broken ergodicity in the EastREM and the GOEastREM, we moved on to investigate whether this broken ergodicity persists under the presence of periodic driving, or if energy injected into the system results in infinite heating at long times. In the latter case, heating would lead to the recovery of ergodicity, and a renewed agreement with the eigenstate thermalisation hypothesis. As we saw, the eigenstates remained localised under driving, indicating the robustness of the broken ergodicity.

Here, we will repeat this investigation, in order to determine whether Stark localised eigenstates maintain their properties under driving. Like we did previously, we will introduce driving to the hopping amplitude via a step function, so that at every half period  $T/2$ , we switch between the two Hamiltonians:

$$H_0 = H(J + \Delta J), H_1 = H(J - \Delta J). \quad (13)$$

Varying the hopping in this way ensures that at large frequency, the effective Floquet Hamiltonian converges to the following form:

$$H_{\text{eff}} = (H_0 + H_1)/2 = H_s, \quad (14)$$

where  $H_s$  is the undriven Hamiltonian.

#### 3.1 Dynamics

First, let's return to the single particle system, and reintroduce the linear potential defined in equation 3. To investigate this system under driving, we will look at both the dynamics and the eigenstates.

The simplest dynamical measure that we can use is the survival function,  $G(t)$ . Recall that  $G(t) = 1$  at all times in a maximally localised system, indicating that memory of the initial state is fully conserved. Conversely, we have  $G(t) = 1/L$  after some finite time in a delocalised system, which indicates that memory of the initial state is lost.

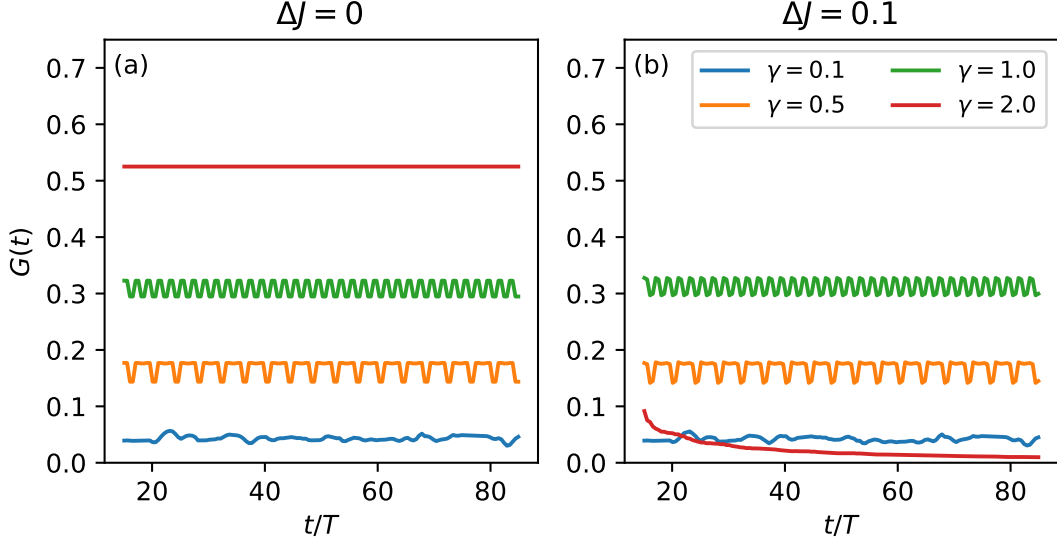


Figure 7: Time evolution of the survival function in a single-particle Stark localised system, with (a) no driving and (b) periodic driving. Parameters are  $J = 1$ ,  $\omega = 2$ ,  $L = 64$ . The state in which the particle is in the middle of the lattice is taken to be the initial state. The noise has been smoothed out using a convolution function.

In figure 7, we plot the dynamics for the survival function for various potential strengths. In (a) we see what the behaviour looks like in the static system (driving amplitude 0), which again demonstrates how the system localises with increasing  $\gamma$ . In (b), we observe the dynamics in the presence of driving, which appears to yield no qualitative change, except at  $\gamma = \omega$ . Here, the survival function appears to drop to the maximally delocalised prediction. It should be noted that this delocalisation fails for states in which the particle is close to the edge of the lattice, which corresponds to the fact that the energy level spacing does not match the potential gradient at the spectral edges. This property corresponds to the 'weak' notion of ergodicity, in which loss of memory is dependent on the initial conditions.

### 3.2 IPRs

Next, we will look at the eigenstates of the Floquet operator, which contain the infinite-time properties of the driven system. We will look to the usual IPRs as a measure of localisation, which have the properties  $I = 1$  in a maximally localised system and  $I = 1/L$  in a maximally delocalised system. These properties mirror those of the survival function, which we recall is because the IPR is, by definition, the infinite-time prediction of the survival function.

We will use this metric to investigate more closely the importance of the driving frequency,  $\omega$ . We will also take the average over all eigenstates, and observe various system sizes with the hope of finding an extrapolation to the thermodynamic limit.

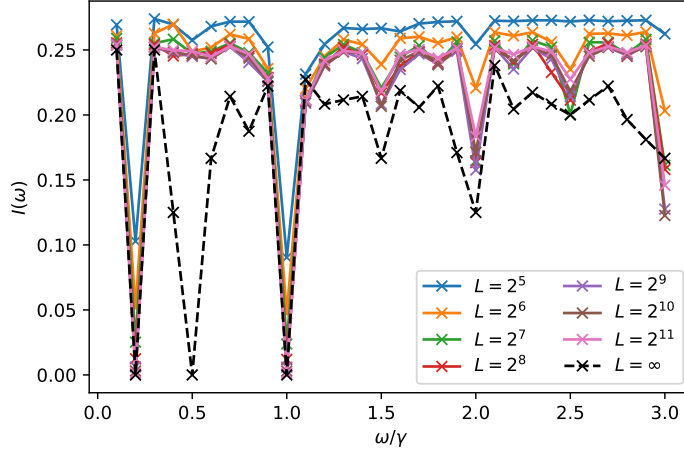


Figure 8: Inverse participation ratio of the periodically driven single particle system, scanned across driving frequency  $\omega$ . Parameters are  $J = 1$ ,  $\Delta J = 0.1$ ,  $\gamma = 1$ . The IPR has been averaged over all eigenvectors. The infinite size prediction is given by equation 15.

We plot the IPRs as a function of  $\omega$  in figure 8. What we can see is that the IPR mostly appears to spike towards the delocalised regime at specific values of  $\gamma$ . In particular, the IPR becomes maximally delocalised at  $\omega/\gamma = 1$  and  $\omega/\gamma = 0.2$ . The IPR also seems to slightly delocalise at integer multiples of  $\gamma$ .

At this point, we can attempt to construct a semi-analytical prediction of the IPRs in the thermodynamic limit using the following reasoning: it is known that periodic driving ensures

that the eigenvalues are mapped into a Brillouin zone of width  $\omega$ . If the width of the Brillouin zone is equal to the spacing between the eigenvalues, then one should expect that each eigenvalue is mapped into the same position in the Brillouin zone, rendering them degenerate. This also explains why setting the frequency to integer multiples of the gradient yields a similar but weaker effect. For example, if  $\omega = 2\gamma$ , eigenvalues that differ by an energy  $\gamma$  will yield quasienergies that also differ by  $\gamma$ . However, eigenvalues that differ by  $2\gamma$  will yield degenerate quasienergies.

Numerically we can replicate this artificially by generating a set of eigenvalues  $\epsilon$  of spacing  $\gamma$ , and mapping them into a Brillouin zone of width  $\omega$  to yield quasienergies  $\alpha_i = \epsilon_i \bmod (\omega)$ . If these quasienergies are exactly degenerate, then the total spacing will be equal to 0, which also equals the maximally delocalised IPR in the thermodynamic limit. Next, one needs to factor in the fact that the number of degenerate groups that the eigenvalues split into generally scales linearly with  $\omega$ . We can deal with this by dividing by a factor of  $\omega$ . Finally, we see in figure 8 that the highest value of  $I(\omega)$  is approximately  $1/4$ , which we can factor in as a constant. From this we can construct the following expression:

$$I(\omega) = \frac{1}{4\omega} \sum_i (\alpha_{i+1}(\omega) - \alpha_i(\omega)). \quad (15)$$

In figure 8, we can see that our infinite size prediction detects all of the significant spikes, albeit at various magnitudes. However, the biggest distinction is the fact that maximal delocalisation is predicted at  $\omega/\gamma = 0.5$  whereas in reality no spike can be seen at all at any finite size.

### 3.3 Localisation Length

It might also be useful to check what the eigenvectors look like in the presence of driving. In figure 1, we saw that the averaged eigenvector is strongly delocalised in the presence of a weak potential, illustrating the proximity to a degenerate regime. Employing the same method, we should expect a similar behaviour in which the eigenvectors look more localised as  $\gamma$  is increased, with exceptions at the spikes seen in figure 8.

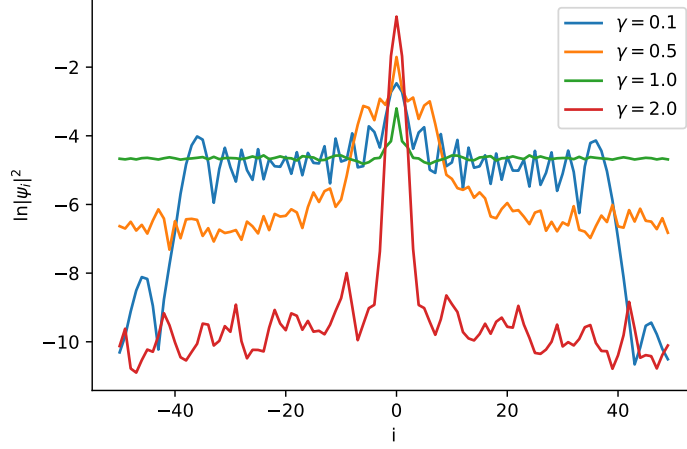


Figure 9: Average distribution of eigenvector weights in a driven single particle system across real space, centred around the site with the largest weight. Parameters are  $L = 200$ ,  $J = 1$ ,  $\Delta J = 0.1$ ,  $\omega = 1$ .

Figure 9 shows the average eigenvector weights for various choices of  $\gamma$ . The weight is shown to be most evenly distributed when  $\gamma = \omega$ , in agreement with the survival function in figure 7(b).

Following from this, we can construct a similar measure as the IPRs in figure 8 by plotting the localisation length as a function of driving frequency. To achieve this, we will need to find a numerical means of calculating the localisation length for a given averaged eigenvector. Looking at e.g. the  $\gamma = 2$  plot in figure 9, the localisation length can be defined by the width of the central peak. Numerically, the easiest way to obtain this is to count the number of sites whose weight satisfies a given threshold. We can define this threshold as approximately the weight above which  $\ln |\psi_j|^2$  sits in the maximally localised case.



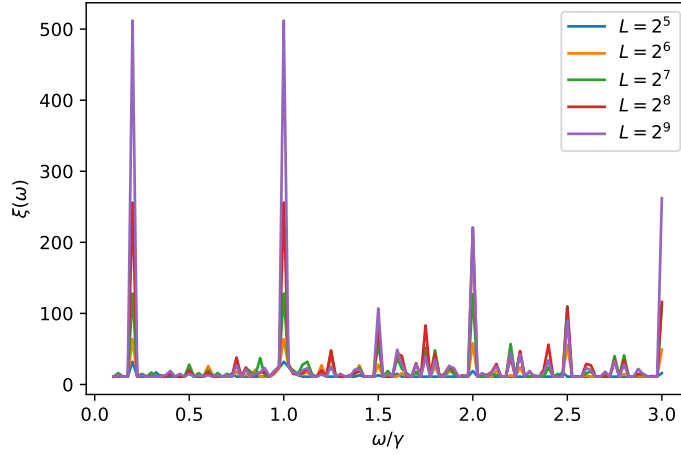


Figure 10: Localisation length of the averaged eigenvector  $\psi_j$  as a function of  $\omega$ . Parameters are:  $J = 1$ ,  $\Delta J = 0.1$ ,  $\gamma = 1$ . The localisation length is defined as the number of sites for which  $\ln |\psi_j|^2 > -7$ .

We plot the localisation length against  $\omega$  in figure 10. At  $\omega/\gamma = 1$  and  $\omega/\gamma = 0.2$  the localisation length is shown to peak suddenly to  $\xi = L$ , indicating that the system is maximally delocalised. More modest peaks are seen at integer values, demonstrating overall strong agreement with the IPRs in figure 8.

### 3.4 Degeneracies Induced by Periodic Driving

So far we have observed that periodic driving delocalises the single particle system specifically if the frequency of the driving equals the gradient of the potential, and therefore the spacing between the energy levels. We argued that this is because the quasienergies of the Floquet operator are remapped onto the same position within the Brillouin zone. Here, we will attempt to gain further insight into this behaviour by following on from a previous theoretical work [22].

In this work, the author invokes Floquet's theorem with the aim of obtaining a general solution to the time-dependent Schrödinger equation with a Hamiltonian that is periodic in time. By expanding the periodic functions into a Fourier series, the Hamiltonian is replaced with a time-independent Hamiltonian with an infinite dimensionality. This Hamiltonian is referred to as

the Floquet Hamiltonian that is associated with the initial time-dependent Hamiltonian, and is defined via its matrix elements:

$$\langle \alpha n | \mathcal{H}_F | m \beta \rangle = \mathcal{H}_{\alpha\beta}^{n-m} + n\omega \delta_{\alpha\beta} \delta_{nm}. \quad (16)$$

Here,  $\alpha$  and  $\beta$  denote the atomic states belonging to the time-dependent Hamiltonian, and  $n$  and  $m$  are the Fourier components. The index of each row and column is thus given by the product  $\alpha n$ . From the RHS, this Hamiltonian has the property that the diagonal elements repeat periodically as one goes along the matrix, but with the addition of an extra factor  $n\omega$  after every instance. For example, a two-level periodic system with diagonal elements  $E_\alpha$  and  $E_\beta$  will possess a corresponding Floquet Hamiltonian with diagonal elements  $E_\alpha, E_\beta, E_\alpha + \omega, E_\beta + \omega, E_\alpha + 2\omega, E_\beta + 2\omega \dots$

In our system, the diagonal elements are spaced by  $\gamma$ . This means that if driving occurs at  $\omega = \gamma$ , then the Floquet Hamiltonian will have diagonal elements of the form  $E, E + \gamma, E + \gamma, E + 2\gamma, E + 2\gamma \dots$ , such that every two energy levels are rendered degenerate by the driving. This gives the single particle system the same delocalising property as the many-particle system in the non-interacting limit: as soon as any perturbation is applied to the system, any unperturbed eigenstates that were initially degenerate become strongly hybridised. If the driving that induces these degeneracies is itself thought of as a perturbation, then the system should be expected to delocalise at exactly the frequencies that create the degeneracies.

## 4 Driven Stark Many-Body Localisation

In the single particle case, we discovered that Wannier-Stark localisation is broken under driving at specific frequencies. This was related to the fact that the eigenvalues are exactly spaced according to the gradient of the tilt,  $\gamma$ . Naturally, one might then wonder whether this behaviour persists in the presence of interactions.

Let us reintroduce the many-body Hamiltonian from equation 12, for a half-filled lattice of hard-core bosons with open boundary conditions. Note that because we are working with hard-core bosons, the model can easily be converted to a spin representation via the Jordan-Wigner transformation, without the need for any string operator that recovers the anticommutation

relations defined in equation 6. From this we obtain

$$H = J \sum_j^{L-1} (S_j^- S_{j+1}^+ + \text{h.c.}) + V \sum_j^{L-1} \left( S_j^z + \frac{1}{2} \right) \left( S_{j+1}^z + \frac{1}{2} \right) + \sum_j^L W_j \left( S_j^z + \frac{1}{2} \right) + \sum_j^L \epsilon_j \left( S_j^z + \frac{1}{2} \right), \quad (17)$$

where the  $S_j^+$  and  $S_j^-$  are ladder operators that raise or lower the spin configuration on site  $j$ , and  $S_j^z$  measures the spin on site  $j$ .

#### 4.1 IPRs

As we did previously, we can investigate the effect of the driving on the eigenstates most directly by looking at the IPRs as a function of driving frequency  $\omega$ . To ensure that the system is localised in the absence of driving, we will implement a strong tilt, such that  $\gamma \gg V$ . To illustrate explicitly the effect of driving on the IPRs, we will also calculate the magnitude of the difference between the average IPR under driving,  $I(\omega)$ , and that of 0 driving,  $I_0$ .

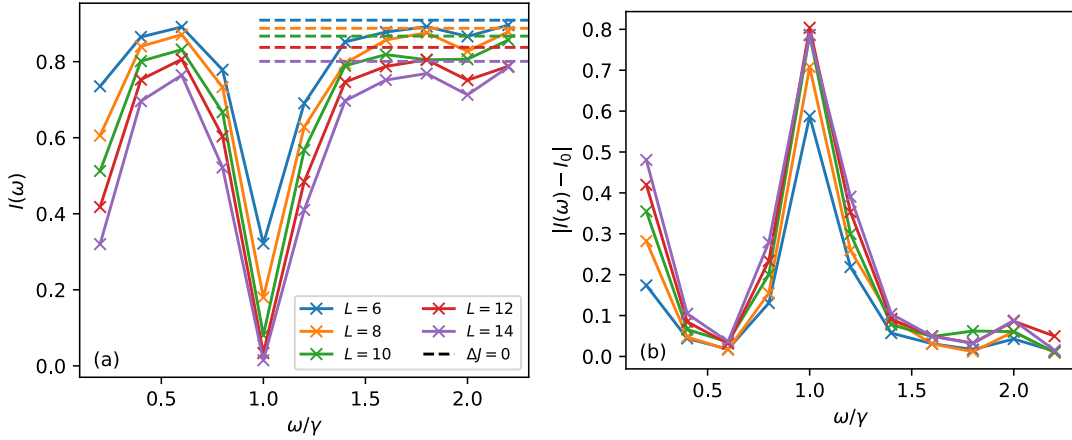


Figure 11: (a) Averaged IPR as a function of driving frequency  $\omega$ , and (b) magnitude of difference between averaged IPR under driving and that of no driving. Parameters are  $V = 0.5$ ,  $J = 0.5$ ,  $\gamma = 5$ ,  $w = 0.05$ ,  $\Delta J = 0.1$ . Averaging takes place over all eigenvectors and  $m$  disorder realisations, where  $m = \text{ceil}(3000/\mathcal{D})$ . The dashed lines in (a) indicate the IPRs in the absence of driving.

In figure 11 we see the effect of driving on the IPRs in the interacting case. At  $\omega/\gamma = 0.5$  it is clear that the driving has very little effect on the eigenstates, whereas at  $\omega/\gamma = 1$  we can see that the system is more strongly delocalised by the driving. In contrast to the single particle case, delocalisation doesn't happen strictly at specific points, but also around them. This is because the interactions split the degeneracies in the non-interacting limit into bands, so that bands whose energies differ by  $\gamma$  are hybridised by the driving at  $\omega = \gamma$ .

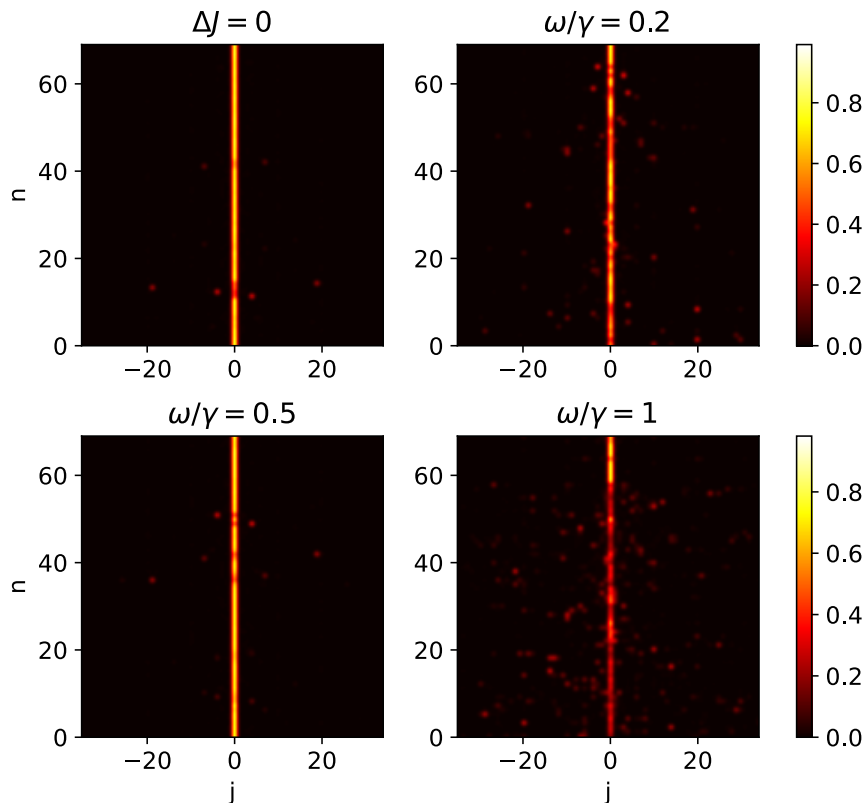


Figure 12: Distribution of all eigenvector weights in the Stark MBL model with both driving and no driving, where  $n$  denotes the eigenvector and  $j$  denotes the weight at Fock site  $j$ . All eigenvectors are shifted so that the site with maximum weight is at  $j = 0$ . Parameters are  $L = 8$ ,  $J = V = 0.5$ ,  $\gamma = 5$ ,  $w = 0.05$ ,  $\Delta J = 0.1$ .

As we did in the single particle case, we should observe how the individual eigenvectors are affected by the driving. Figure 12 demonstrates the effect on the individual eigenvectors under driving. As the IPRs suggest, driving at  $\omega/\gamma = 0.5$  has very little effect on the eigenvectors,

whereas driving at  $\omega/\gamma$  significantly reduces the amplitude of the central peak. In particular, instead of the peak simply broadening we see the emergence of multifractality within the eigenvectors.

One might wonder why the IPRs in the undriven case decrease with system size, which should immediately look strange if one assumes that the system is strongly in the Stark MBL regime. The reason for this is likely related to the non-trivial structure of the eigenstates, where although they are all sharply peaked around a single Fock state, many of them still possess smaller peaks with significant weight. This is demonstrated in the undriven picture in figure 12, where significant support can be seen in regions outside of the primary peak. The resulting property of the IPRs seems consistent with the observation that the time taken for a Stark MBL system to delocalise increases with system size, implying that such systems are only truly localised in the thermodynamic limit [19].

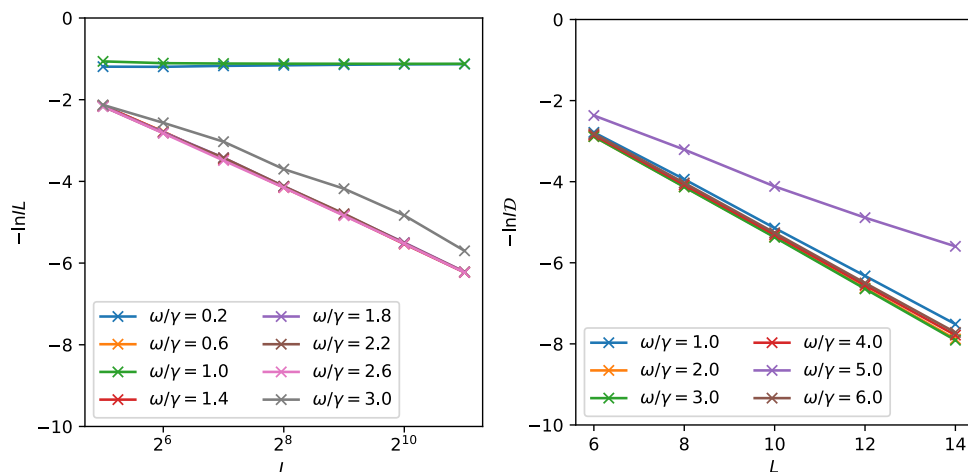


Figure 13: Log of fraction of occupied Hilbert space for averaged IPRs under driving in (a) the single particle system and (b) the interacting system. The IPRs are taken from figures 8 and 11, respectively.

When an IPR decreases with system size, it is not clear whether this implies that the system is becoming more localised, because the maximally delocalised value of  $1/\mathcal{D}$  is also decreasing. Therefore, one can check more closely the approach of the IPR to the thermodynamic limit by instead calculating  $1/I\mathcal{D}$ , which is the participation ratio – i.e. the number of Fock states

contributing to the eigenstates – relative to the dimensionality. This gives the fraction of Hilbert space occupied by an eigenstate [23]. In an Anderson localised system of dimensionality  $L$ , the localisation length is independent of system size, so we should expect a scaling of  $1/IL \propto 1/L$ , or  $-\ln IL \propto -\ln L$ . Otherwise, we should expect  $-\ln IL$  to be independent of system size, which ensures that a finite fraction is occupied in the thermodynamic limit.

In figure 13, we plot the log of the fraction of occupied Hilbert space for the averaged IPRs in both the single particle system and the interacting system. In (a) we can see that the fraction decreases with the expected  $L$ -dependence of a localised system, except at the specific frequencies  $\omega/\gamma = 0.2$  and  $\omega/\gamma = 1$ , indicating that at these frequencies the system is delocalised in the thermodynamic limit. Conversely, in (b) we can see that all fractions decrease with  $L$ , including at  $\omega/\gamma = 1$ . This might suggest that the system localises in the thermodynamic limit, but it is also possible that this  $L$ -dependence is a finite-size effect. In principle one would therefore need to obtain the first derivative of this metric with respect to  $L$  to get a clear picture of whether the system is delocalised, which would require extreme numerical precision.

One could also argue that the intermediate behaviour observed is a signature of the multifractality implied in figure 12. It might therefore be helpful to employ a tool that is able to measure multifractality more directly.

## 4.2 Multifractality

In order to investigate the multifractality of our model under driving, we can employ a standard measure derived from the generalised IPRs. Recall that for an eigenvector  $|\epsilon\rangle$  these are defined as

$$I_q = \sum_i |\langle \epsilon | i \rangle|^{2q}. \quad (18)$$

The standard IPR that we have been using so far are thus  $I_q$  at  $q = 2$ . If the  $I_q$  scale with the dimensionality  $I_q \sim \mathcal{D}^{-\tau_q}$ , then the scaling exponent  $\tau_q$  is defined as

$$\tau_q = -\frac{\ln I_q}{\ln \mathcal{D}}. \quad (19)$$

As we have been doing so far, we will calculate the IPRs by first averaging over all eigenvectors – after shifting them in terms of the location of their maximum weight – and also averaging over disorder. Following on from [24], we will extrapolate the scaling exponent at each  $q$  to infinite size

by plotting  $\tau_q$  against  $1/\ln \mathcal{D}$ . This procedure is demonstrated in figures 14(a) and (d), which correspond to driving at  $\omega/\gamma = 1$  and  $\omega/\gamma = 0.5$ , respectively. The correctness of this procedure is apparent at smaller values of  $q$  in figure (a), whereas a departure from linear dependence can be seen at larger values. This implies that for larger sizes the extrapolation will increase more at large  $q$ .

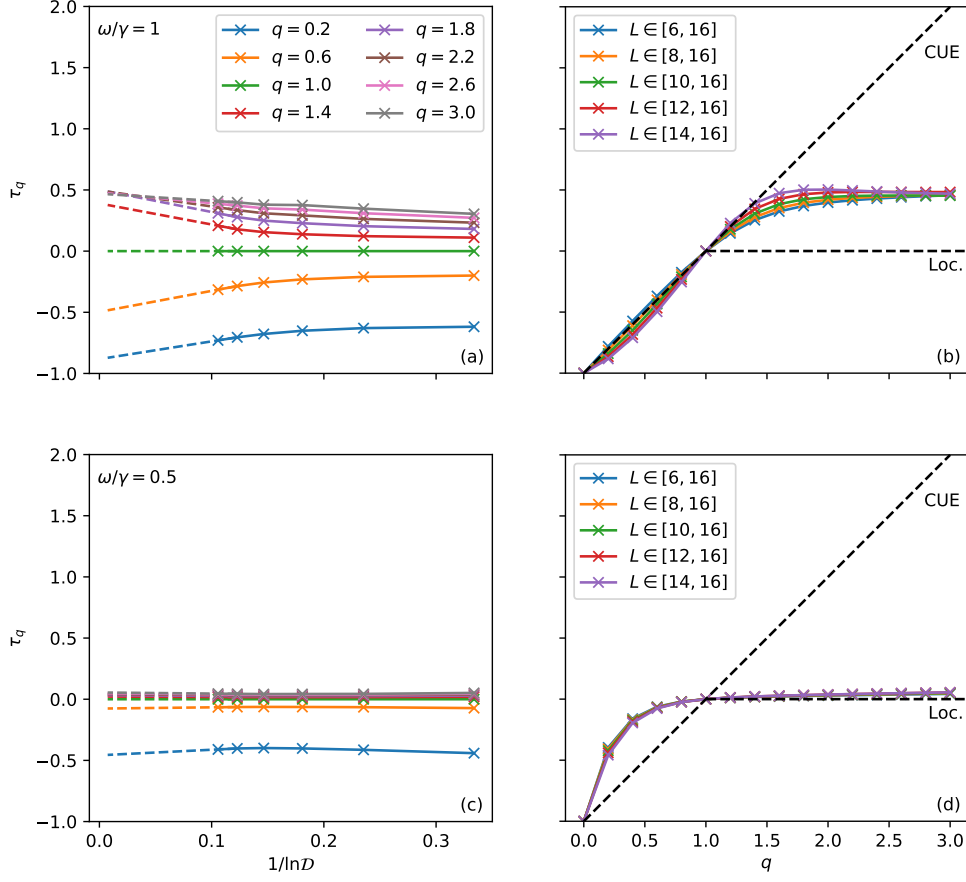


Figure 14: Averaged scaling exponent  $\tau_q$  for the driven Stark MBL system. Figures (a) and (c) shows the extrapolation of  $\tau_q$  to infinite size via plotting against  $1/\ln \mathcal{D}$ . Figures (b) and (d) show the extrapolated scaling exponents via interpolations between various pairs of system sizes, where  $L \in [a, b]$  denotes an interpolation between sizes  $a$  and  $b$ . Figures (a) and (b) correspond to driving at  $\omega = \gamma$  and (c) and (d) correspond to  $\omega = \gamma/2$ . Parameters are  $J = V = 0.5$ ,  $\gamma = 5$ ,  $w = 0.05$ ,  $\Delta J = 0.1$ . Averaging takes place over  $n$  disorder realisations, where  $n = \text{ceil}(5000/\mathcal{D})$ .

In figures 14(b) and (d), we plot the extrapolated values against  $q$  using all possible extrapolations between the largest size and the remaining sizes. For  $q \leq 1$ , the  $\tau_q$  universally converge to  $q - 1$ . At  $q = 1$ , the corresponding IPR is just the total weight of the eigenvector components, which



yields a log of 0 by normalisation. At  $q = 0$ , the IPR is the dimensionality, yielding  $\tau_0 = -1$ . In a localised system, one expects that  $\tau_q = 0 \forall q \geq 1$ . This is demonstrated quite strongly in figure (d). Conversely, for a GOE matrix, the prediction is  $\tau_q = q - 1$ . In figure (b), we see agreement with the GOE prediction up to some value  $q^*(L)$ . The departure above  $q^*(L)$  implies multifractality at these higher moments, however the increase of  $q^*(L)$  with system size might also imply that this is a finite effect. Nonetheless, it is also possible that  $q^*(L)$  might saturate at some large  $q$ , confining the multifractality to large moments in the thermodynamic limit [24]. In either case, there is no convergence towards the localised regime, which supports the scenario in which the Hilbert space fraction saturates at some finite  $L$ .

### 4.3 Dynamics

So far in our driven systems we have looked at the properties of the eigenstates. To support these results we will turn now to the dynamics. As with the EastREM, simulating dynamics brings with it the numerical advantage of not needing to diagonalise or even generate the Floquet operator. As a result, we can access significantly larger system sizes. A common dynamical signature of MBL is logarithmic spreading of entanglement, in contrast to the ballistic spread seen in ergodic systems.

As we did in the static system, we will calculate the bipartite entanglement entropy expressed in equation 11, where subsystems  $A$  and  $B$  constitute the left and right halves of the lattice, respectively. Using matrix exponentiation in scipy's sparse library, we can simulate dynamics up to size  $L = 22$ . The system will be prepared in the Néel state, in which the total nearest-neighbour interaction is 0.

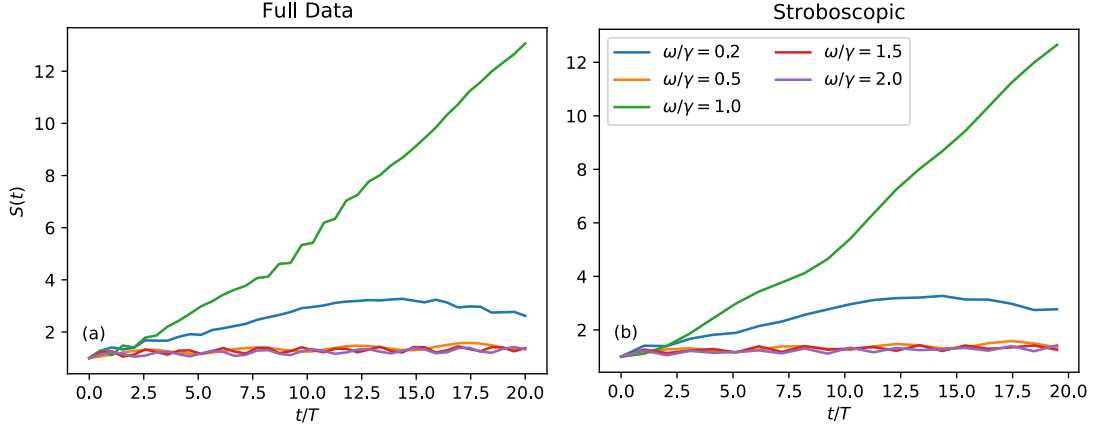


Figure 15: Time evolution of the bipartite entanglement entropy, in the driven Stark MBL system. In (a) we show the entropy at every time increment, whereas in (b) we show only the first increment of each period, and interpolate between them. Other parameters are  $L = 22$ ,  $J = V = 0.5$ ,  $\gamma = 5$ ,  $w = 0.05$ ,  $\Delta J = 0.1$ .

In figure 15 we plot the bipartite entanglement entropy across time, for several driving frequencies. Predictably, we see that the entropy grows slower for increasing  $\gamma$ , except at the resonant point where much faster growth is seen. Here, the growth appears to be mostly linear, indicating volume law scaling.

#### 4.4 Driven Field vs Driven Hopping

Another degree of freedom in driven Stark MBL is the choice of which parameter to drive. Currently we have been driving the hopping,  $J$ , at sufficiently small amplitude such that  $J + \Delta J \ll \gamma$ . This way, we have been able to probe for the possibility of delocalising the system by way of resonant driving, while avoiding the limit of simply overcoming the tilted potential via sufficient heating.

With this consideration, one might wonder whether such a limit would persist if one were to drive the gradient of the tilt, rather than the hopping. To investigate this, we can employ the initial form of driving, but define the Hamiltonians at each half period such that

$$H_0 = H(\gamma + \Delta\gamma), H_1 = H(\gamma - \Delta\gamma), \quad (20)$$

where  $\Delta\gamma$  is the amplitude of the drive.

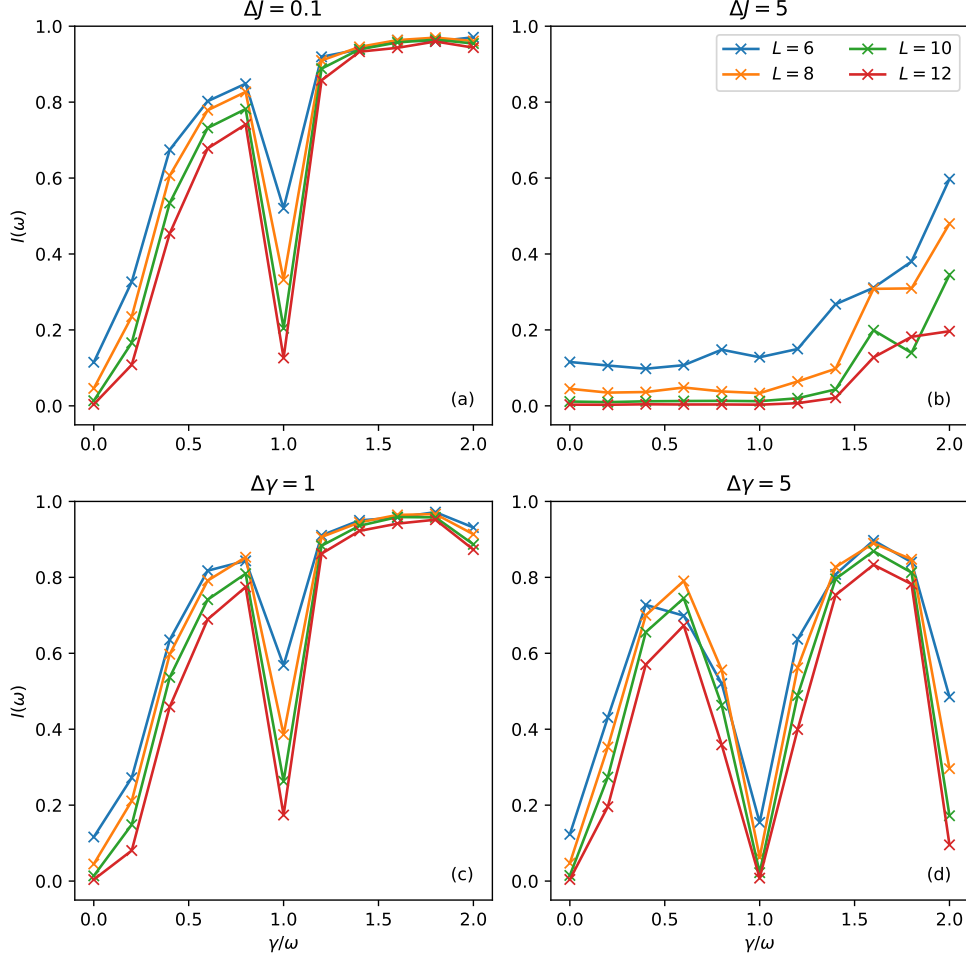


Figure 16: Averaged IPR scanned across tilt  $\gamma/\omega$ , for (a) and (b) driven hopping and (c) and (d) driven tilt. Parameters are  $J = V = 0.5$ ,  $\omega = 6$ ,  $w = 0.05$ . Averaging takes place over all eigenvectors and  $m$  disorder realisations, where  $m = \text{ceil}(1000/\mathcal{D})$ .

In figure 16 we compare the effect of driving between both hopping and tilt, by scanning the averaged IPR across the average strength of the tilt,  $\gamma$ . The effect of small driving is shown in (a) and (c), where the system trivially localises in the limit  $\gamma \gg J$  and delocalises at  $\gamma \ll J$ . At the resonant point, we see the delocalisation that has been previously demonstrated. In (b), we see how driving the hopping at large amplitudes trivially delocalises the system at all  $\gamma$  away from the  $\gamma \gg J$  limit. In (d) however, we observe very different behaviour. Here, driving the

field at large amplitudes does not trivially delocalise the system, but actually reveals another resonant point at  $\gamma/\omega = 2$ .

This confirms that under field driving, there is no limit of trivial heating for  $\Delta\gamma \gg \gamma$ . Without this limit, one is granted the advantage of being able to amplify the resonant effects by maximising the amplitude, revealing additional resonant points at large  $\gamma$ .

## 4.5 Alternative Driving

In order to achieve cleaner IPRs as a function of driving frequency, one could instead consider driving in the following way:

$$H(t) = \begin{cases} H_0, & t \leq T_0 \\ H_1, & T_0 < t \leq T_0 + T_1, \end{cases} \quad (21)$$

where  $H_0$  is the diagonal part of the stationary Hamiltonian and  $H_1$  is the off-diagonal part. The associated Floquet operator is then

$$\mathcal{F} = e^{-iH_0T_0}e^{-iH_1T_1}. \quad (22)$$

Here, the period of the driving is  $T = T_0 + T_1$ , where  $T_0$  is the period over which  $H(t) = H_0$  and  $T_1$  is the period over which  $H(t) = H_1$ . At  $t \leq T_0$ , the off-diagonal elements are set to 0, in which case the system is trivially localised given that the Fock states are now eigenstates. This means that in the limit  $T_1 \ll T_0$ , we have  $H(t) \approx H_0$ , in which case the system will be strongly localised. Conversely, in the limit  $T_1 \gg T_0$ , we have  $H(t) \approx H_1$ , which corresponds to strong driving if  $J/V$  is not too small. Since we aren't interested in the effect of strong driving, we need to ensure that we remain in the limit  $T_1 \ll T_0$  for all  $\omega$ . But given that we also need to satisfy  $T_0 < T$ , it would make sense to set  $T_1$  as a constant, such that  $T_1 \ll T$ .

An extra complication here is the fact that the time-dependence is no longer constrained to the off-diagonal elements. This means that we cannot cast  $H(t)$  into the time-independent picture demonstrated by Shirley, until we express it in a form in which the time-dependence only exists in the off-diagonal elements [22]. One way to achieve this is to rewrite our Hamiltonian as

$$H(t) = \bar{H} + \delta H(t), \quad (23)$$

where  $\bar{H}$  is the time average of  $H(t)$ , and  $\delta H(t)$  is the oscillating part of  $H(t)$ . First, we calculate  $\bar{H}$  as:

$$\bar{H} = \frac{1}{T} \int_0^{T_0} H_0 dt + \frac{1}{T} \int_{T_0}^T H_1 dt = \frac{H_0 T_0}{T} + \frac{H_1 T_1}{T}. \quad (24)$$

This can be expressed fully as

$$\bar{H} = \tilde{J} \sum_j^{L-1} (b_j b_{j+1}^\dagger + \text{h. c.}) + \tilde{V} \sum_j^{L-1} n_j n_{j+1} + \sum_j^L \tilde{\gamma} j n_j + \sum_j^L \tilde{\epsilon}_j n_j, \quad (25)$$

where  $\tilde{J} = JT_1/T$ ,  $\tilde{V} = VT_0/T$ ,  $\tilde{\gamma} = \gamma T_0/T$ , and  $\tilde{\epsilon}_j = \epsilon_j T_0/T$ .

Meanwhile, we can express the time-dependent part as

$$\delta H(t) = H(t) - \bar{H} = \begin{cases} H_0 \left(1 - \frac{T_0}{T}\right) - \frac{H_1 T_1}{T}, & t \leq T_0 \\ H_1 \left(1 - \frac{T_1}{T}\right) - \frac{H_0 T_0}{T}, & T_0 < t \leq T_0 + T_1. \end{cases} \quad (26)$$

Now that the time dependence is confined to  $\delta H(t)$ , our Hamiltonian can be recast into the Shirley picture. In the case of the previous driving, we found that adjacent energy bands – corresponding to the diagonal part of the Floquet Hamiltonian – become strongly coupled if  $\omega = \gamma$ . In our case, we should expect this same behaviour at  $\omega = \tilde{\gamma}$ . Having set  $T_1$  as a constant, this gives us

$$\frac{2\pi}{T} = \frac{\gamma T_0}{T}, T_0 = \frac{2\pi}{\gamma}. \quad (27)$$

Thus, we should expect that the system delocalises at  $T_0 = \frac{2\pi}{\gamma}$ . To check this numerically, we will scan across  $T_0$  and normalise the parameter as  $\gamma T_0/2\pi$ , meaning that delocalisation should be expected at 1.

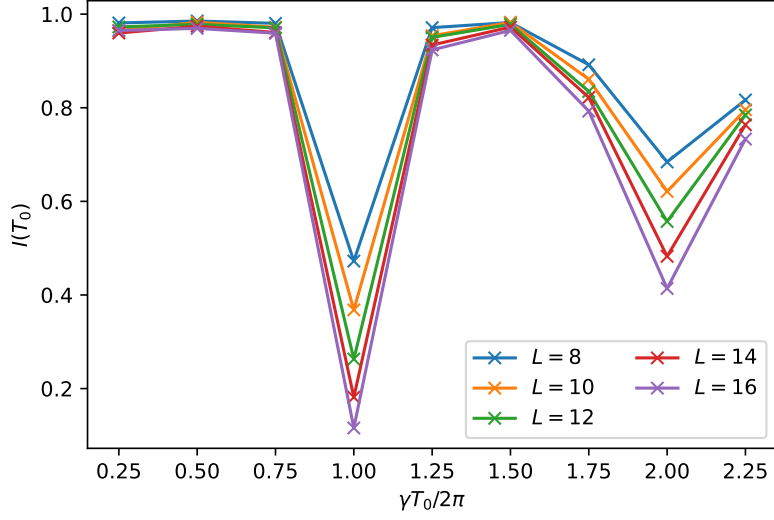


Figure 17: Averaged IPR as a function of driving frequency  $\omega$  for the driving defined in equation 21. Parameters are the same as in figure 11, with  $T_1 = 0.05$ . Averaging takes place over all eigenvectors and  $m$  disorder realisations, where  $m = \text{ceil}(10^4/\mathcal{D})$ .

Figure 17 shows driving of the system via equation 21. Comparing with the IPRs in figure 11, we see the same qualitative behaviour in which the system is generally localised, except at the resonant point  $\gamma T_0/2\pi = 1$ . However, now we can also see a second resonant point at  $\gamma T_0/2\pi = 2$ . Another important distinction is that the system appears to be fully localised away from the resonant points at all sizes.

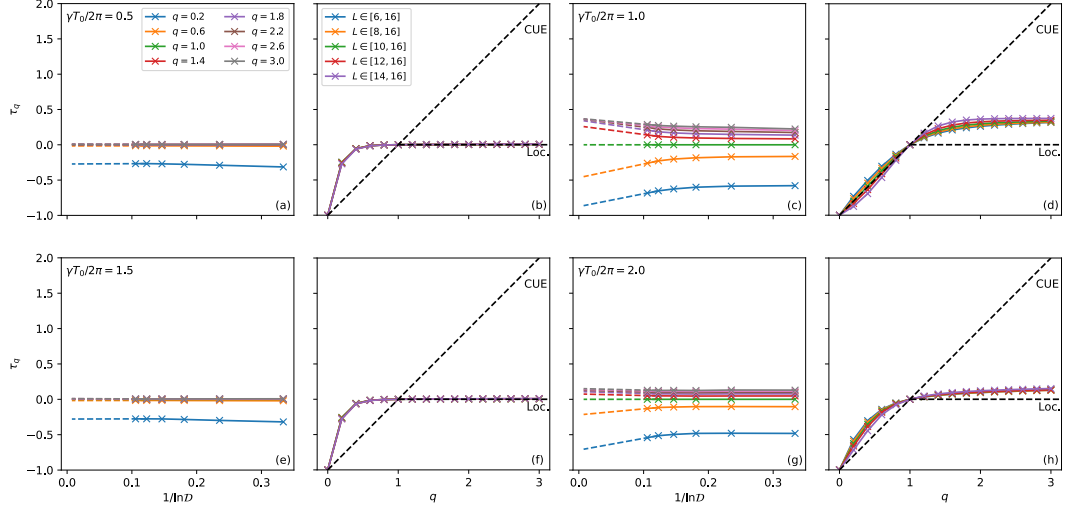


Figure 18: Averaged scaling exponent similar to figure 14, for a system driven according to equation 21. Parameters are the same as in figure 11, with  $T_1 = 0.1$ . Averaging takes place over all eigenvectors and  $m$  disorder realisations, where  $m = \text{ceil}(3000/\mathcal{D})$ .

Let us also look again at the scaling exponent at both the resonant point and away from the resonant point according to this new driving. In figure 18, we plot the scaling exponent for (a), (b), (i) and (j) at the resonant points and away from the resonant point otherwise. Just as we see in figure 14, the extrapolated scaling exponent obeys the prediction for a localised system at all  $q$ , whereas at the resonant point the system follows the CUE prediction up to  $q = 1$ , before deviating.

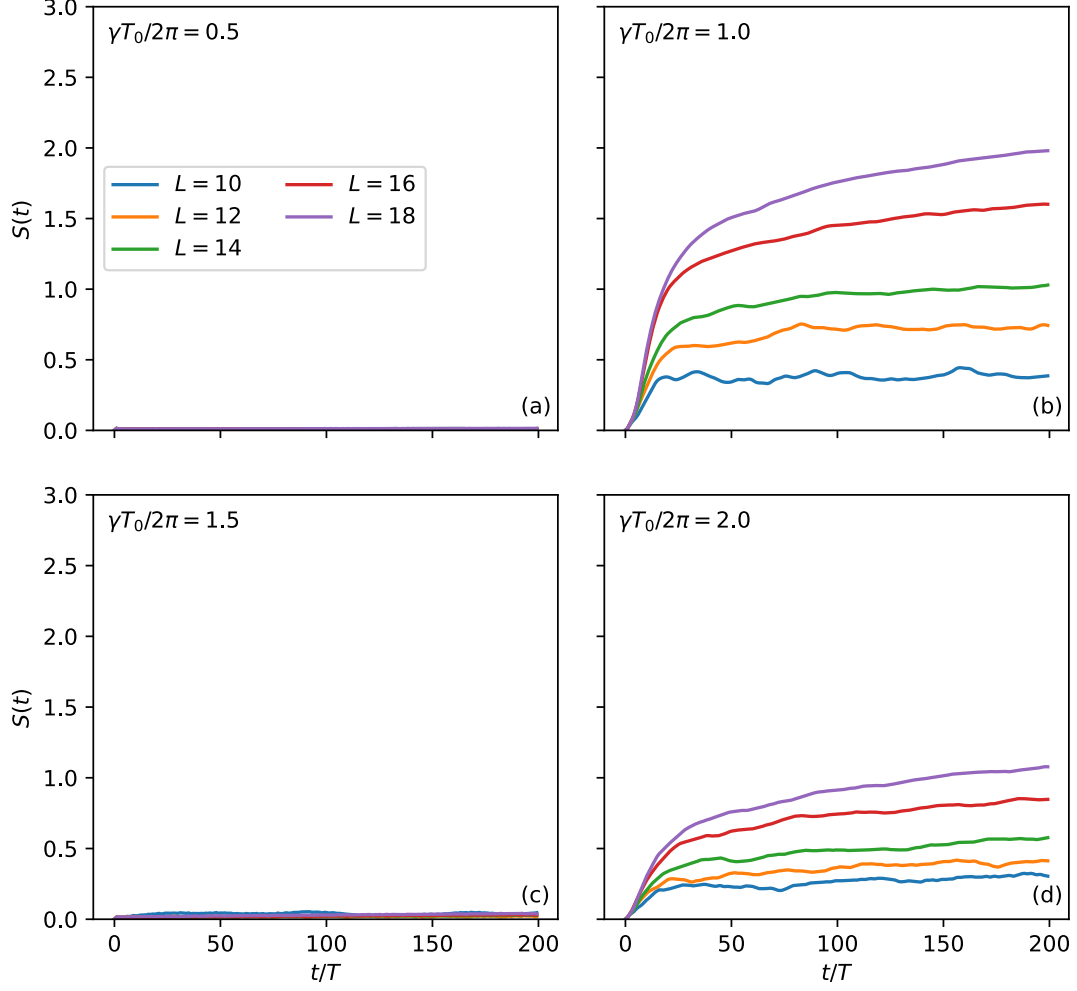


Figure 19: Time evolution of bipartite entropy under cleaner form of driving. (b) and (d) depict the time evolution at the resonant points, while (a) and (c) depict the evolution away from the resonant points. The time evolution shown in all cases is stroboscopic, as in figure 15(b).

We can also return to the time evolution of the bipartite entanglement entropy via the cleaner form of driving. We plot the data for this in figure 19. At the resonant points, it is clear that the entropy evolves towards some finite equilibrium value that increases with system size. Meanwhile, away from the resonant points the entropy remains at 0 for all sizes at all times.



## References

- [1] Gregory H Wannier. Dynamics of band electrons in electric and magnetic fields. *Reviews of Modern Physics*, 34(4):645, 1962.
- [2] Maximilian Schulz, CA Hooley, Roderich Moessner, and F Pollmann. Stark many-body localization. *Physical review letters*, 122(4):040606, 2019.
- [3] Evert van Nieuwenburg, Yuval Baum, and Gil Refael. From bloch oscillations to many-body localization in clean interacting systems. *Proceedings of the National Academy of Sciences*, 116(19):9269–9274, 2019.
- [4] Andrea Tomadin, Riccardo Mannella, and Sandro Wimberger. Many-body interband tunneling as a witness of complex dynamics in the bose-hubbard model. *Physical review letters*, 98(13):130402, 2007.
- [5] Ignacio Garcia-Mata and Dima L Shepelyansky. Nonlinear delocalization on disordered stark ladder. *The European Physical Journal B*, 71(1):121–124, 2009.
- [6] Vedika Khemani, Michael Hermele, and Rahul Nandkishore. Localization from hilbert space shattering: From theory to physical realizations. *Physical Review B*, 101(17):174204, 2020.
- [7] Pablo Sala, Tibor Rakovszky, Ruben Verresen, Michael Knap, and Frank Pollmann. Ergodicity breaking arising from hilbert space fragmentation in dipole-conserving hamiltonians. *Physical Review X*, 10(1):011047, 2020.
- [8] Scott Richard Taylor, Maximilian Schulz, Frank Pollmann, and Roderich Moessner. Experimental probes of stark many-body localization. *Physical Review B*, 102(5):054206, 2020.
- [9] Loïc Herviou, Jens H Bardarson, and Nicolas Regnault. Many-body localization in a fragmented hilbert space. *Physical Review B*, 103(13):134207, 2021.
- [10] Qiujiang Guo, Chen Cheng, Hekang Li, Shibo Xu, Pengfei Zhang, Zhen Wang, Chao Song, Wuxin Liu, Wenhui Ren, Hang Dong, et al. Stark many-body localization on a superconducting quantum processor. *Physical review letters*, 127(24):240502, 2021.
- [11] Elmer Guardado-Sanchez, Alan Morningstar, Benjamin M Spar, Peter T Brown, David A Huse, and Waseem S Bakr. Subdiffusion and heat transport in a tilted two-dimensional fermi-hubbard system. *Physical Review X*, 10(1):011042, 2020.

- [12] Sebastian Scherg, Thomas Kohlert, Pablo Sala, Frank Pollmann, Bharath Hebhe Madhusudhana, Immanuel Bloch, and Monika Aidelsburger. Observing non-ergodicity due to kinetic constraints in tilted fermi-hubbard chains. *Nature Communications*, 12(1):1–8, 2021.
- [13] Ling-Na Wu and André Eckardt. Bath-induced decay of stark many-body localization. *Physical Review Letters*, 123(3):030602, 2019.
- [14] Sanjay Moudgalya, Abhinav Prem, Rahul Nandkishore, Nicolas Regnault, and B Andrei Bernevig. Thermalization and its absence within krylov subspaces of a constrained hamiltonian. In *Memorial Volume for Shoucheng Zhang*, pages 147–209. World Scientific, 2022.
- [15] Ruixiao Yao and Jakub Zakrzewski. Many-body localization of bosons in an optical lattice: Dynamics in disorder-free potentials. *Physical Review B*, 102(10):104203, 2020.
- [16] Li Zhang, Yongguan Ke, Wenjie Liu, and Chaohong Lee. Mobility edge of stark many-body localization. *Physical Review A*, 103(2):023323, 2021.
- [17] Christian Klöckner, Christoph Karrasch, and Dante Marvin Kennes. Nonequilibrium properties of berezinskii-kosterlitz-thouless phase transitions. *Physical Review Letters*, 125(14):147601, 2020.
- [18] Alessio Lerose, Federica M Surace, Paolo P Mazza, Gabriele Perfetto, Mario Collura, and Andrea Gambassi. Quasilocalized dynamics from confinement of quantum excitations. *Physical Review B*, 102(4):041118, 2020.
- [19] Guy Zisling, Dante M Kennes, and Yevgeny Bar Lev. Transport in stark many body localized systems. *arXiv preprint arXiv:2109.06196*, 2021.
- [20] Vadim Oganesyan and David A Huse. Localization of interacting fermions at high temperature. *Physical review b*, 75(15):155111, 2007.
- [21] Elmer VH Doggen, Igor V Gornyi, and Dmitry G Polyakov. Stark many-body localization: Evidence for hilbert-space shattering. *Physical Review B*, 103(10):L100202, 2021.
- [22] Jon H Shirley. Solution of the schrödinger equation with a hamiltonian periodic in time. *Physical Review*, 138(4B):B979, 1965.
- [23] Andrea De Luca and Antonello Scardicchio. Ergodicity breaking in a model showing many-body localization. *EPL (Europhysics Letters)*, 101(3):37003, 2013.

- [24] David J Luitz, Ivan Khaymovich, and Yevgeny Bar Lev. Multifractality and its role in anomalous transport in the disordered xxz spin-chain. *SciPost Physics Core*, 2(2):006, 2020.